



## Research Article

## Exploring the amorphous phase formation and properties of W-Ta-(Cr, Fe, Ni) high-entropy alloy gradient films via a high-throughput technique

Yasong Li<sup>a</sup>, Jiang Ma<sup>b</sup>, Peter K. Liaw<sup>c</sup>, Yong Zhang<sup>a,d,e,\*</sup><sup>a</sup> Beijing Advanced Innovation Center of Materials Genome Engineering, State Key Laboratory for Advanced Metals and Materials, University of Science and Technology Beijing, Beijing 100083, China<sup>b</sup> Shenzhen Key Laboratory of High Performance Nontraditional Manufacturing, College of Mechatronics and Control Engineering, Shenzhen University, Shenzhen 518060, China<sup>c</sup> Department of Materials Science and Engineering, The University of Tennessee, Knoxville, TN 37996, USA<sup>d</sup> Qinghai Provincial Key Laboratory of New Light Alloys, Qinghai Provincial Engineering Research Center of High Performance Light Metal Alloys and Forming, Qinghai University, Xining 810016, China<sup>e</sup> Shunde Graduate School of University of Science and Technology Beijing, Foshan 528399, China

## ARTICLE INFO

## Article history:

Received 27 January 2022

Received in revised form 27 March 2022

Accepted 1 May 2022

Available online 4 May 2022

## Keywords:

Compositional gradient high-entropy films

Nanoindentation hardness

Elastic modulus

Composition design

High-throughput technique

Phase-formation rules

## ABSTRACT

A high-throughput technique can realize fast and efficient material screening, and greatly improve the discovery efficiency of advanced materials. In the present work, the gradient composition films of the W-Ta-CrFeNi high-entropy alloy were prepared by the three-target magnetron co-sputtering technique. The gradient alloy films exhibited a body-centered-cubic (BCC) structure near the W or Ta element target, and an amorphous structure near the CrFeNi target region. Considering the effect of the undercooling degree, the amorphous formation region (using  $\Omega \sim \delta$ ) was larger than that of the bulk alloys. These alloy films displayed ultra-high nano-indentation hardness, with the maximum hardness reaching  $\sim 20.6$  GPa. The elastic modulus in the high-entropy composition region was lower than that in the low-entropy composition region. There is a nonlinear relationship between the nano-indentation hardness and mix-entropy of the alloys. This study provides a reference and alternative material library for the development of high-performance advanced materials.

© 2022 Elsevier B.V. All rights reserved.

## 1. Introduction

As a new type of material, high-entropy alloys present excellent properties and become a research hotspot [1–7]. However, since the multi-dimensional compositional space is practically infinite, only tiny regions have been investigated, and the traditional trial and error method is being greatly limited [8–12]. Therefore, the high-throughput technique greatly improves the development efficiency of high-entropy alloys [13]. In recent years, it has developed a variety of methods to achieve high-throughput preparation, including the magnetic co-sputtering coatings [14–17], super-gravity technology [18,19], honeycomb structure [20], 3D-printing technology [21,22], diffusion technology [23], and analog calculation [24–26], etc.

As an efficient thin-film preparation technology, the magnetron sputtering is widely applied to realize the preparation of thin-film materials with a uniform composition by a rotating substrate [17,27–33]. However, upon a stationary substrate, the films with gradient compositions could be achieved with varying the distance and sputtering yield between the substrate regions and the targets. The high-throughput technique via the thin-film enables the rapid preparation materials [14]. Zhang et al. [14] investigated the Ti-Al-(Cr, Fe, Ni) pseudo-ternary high-entropy films, and found a nonlinear correlation among their properties, mixing entropy, and cost performance. Yan et al. [16] prepared a Ti-Zr-Nb alloy film system, using the three-target magnetic sputtering with masking, and screened a low-modulus and medium-entropy alloy,  $Ti_{34}Zr_{52}Nb_{14}$ , with a minimum modulus of 76.5 GPa, which exhibits excellent corrosion resistance in phosphate buffered saline (PBS). Furthermore, Huang et al. reported a research work found that the  $Zr_{52}Ti_{34}Nb_{14}$  alloy film could be prepared employing structurally-flexible films with good wettability [34]. The latest research results presented that after the selected components were introduced into bulk samples, the alloy still displayed excellent comprehensive mechanical properties and

\* Corresponding author at: Beijing Advanced Innovation Center of Materials Genome Engineering, State Key Laboratory for Advanced Metals and Materials, University of Science and Technology Beijing, Beijing 100083, China.

E-mail address: [drzhang@ustb.edu.cn](mailto:drzhang@ustb.edu.cn) (Y. Zhang).

corrosion resistance in PBS [35,36]. Xing et al. [15,37] investigated the magnetic sputtering (Cr, Fe, V)-(Ta, W) pseudo binary high-entropy system, and found that the nanoindentation hardness values of these samples increased with the annealing under 600 °C for 0.5 h. Besides, the Ta<sub>42</sub>W<sub>40</sub>Cr<sub>6</sub>Fe<sub>6</sub>V<sub>6</sub> alloy was reported to show the highest solar absorptivity among the verified compositions. All these previous studies indicated that the high-throughput technique was an excellent pathway to efficiently screen the desired alloys.

Recently, a series of high-entropy alloys containing tungsten or tantalum with high hardness have been reported [38]. Senkov et al. [39,40] investigated the WNbMoTa and WNbMoTaV refractory high-entropy alloys with ultra-high hardness and high-temperature strength. Zou et al. [41] found that the NbMoTaW nano-scale pillar showed excellent properties at room temperature with a yield strength of ~ 10 GPa and stability at high temperatures. Zhang et al. [42] investigated the VCrFeTa<sub>x</sub>W<sub>x</sub> high-entropy alloy and found that the alloy possessed an ultra-high hardness, and high compression strengths at room and elevated temperatures. In addition, the W<sub>38</sub>Ta<sub>36</sub>Cr<sub>15</sub>V<sub>1</sub> high-entropy film shows a high hardness (~ 14 GPa). Simultaneously, it exhibited excellent anti-irradiation hardness at high temperatures [43]. Liu et al. [44] investigated the WFeNiMo high-entropy alloys, showing a stronger self-sharpening than the conventional W-based alloys. Previous studies reported that the CoCrNbNiW laser molten coating possessed excellent wear resistance [45]. Therefore, these alloys could obtain excellent integrated performance by adding refractory elements which have a positive effect on the melting point, and Cr, Fe, and Ni elements widely used in the conventional alloys [33,46–48]. However, the current studies only involve a few alloy compositions. The high-throughput technical screening could efficiently determine the compositions of advanced ultra-hard alloys. In the present work, the W-Ta-CrFeNi multi-component alloy films were prepared by the high-throughput technique with the three-target co-magnetron sputtering. Furthermore, the amorphous phase formation and nanoindentation properties were investigated, based on these gradient alloy films.

## 2. Method

The W-Ta-CrFeNi alloy gradient films were prepared by GJP560, using a three-target magnetron sputtering systems with a diameter of 75 mm and a thickness of 4 mm. The W and Ta targets had a purity of 99.95 wt percent (wt%). The CrFeNi target with a molar ratio of 1:1:1 was prepared by induction melting with 99.95 wt% of Cr, Fe, and Ni. The three targets were 120° apart, focusing on 32 stable silicon wafers [p-Si (1 0 0), 10 mm × 10 mm in size and 10 mm interval], and fixed on a substrate with φ of 150 mm. Fig. 1 shows the schematic diagrams of the alloy target, magnetron-sputtering process and the W-Ta-CrFeNi pseudo-ternary gradient film sample. The samples were synthesized under an Ar atmosphere with a pressure of 0.8 Pa, a flow rate of 60 standard cubic centimeters per minute (scm), a working distance of 50 mm, a deposition time of 45 min, and a working power of 100 W. The substrate stage is fixed during the deposition, and the difference in the deposition density on the substrate could be applied to obtain films with gradient composition.

The microstructure and composition of the W-Ta-CrFeNi gradient film were carried out with a Zeiss SUPRA 55 Scanning Electron Microscope (SEM) and energy dispersive spectroscopy (EDS). The microscope-operating condition was set at an aperture size of 60 μm, low voltage of 15 kV, and working distance of 8 mm, using the secondary electronic detector. The cross-section of the sample was prepared by cleaving off the film from a single crystal silicon substrate, and then used for the thickness detection. The thickness of the films was measured with SEM, and the microscope-operating condition was set at an aperture size of 60 μm, a low voltage of 15 kV,

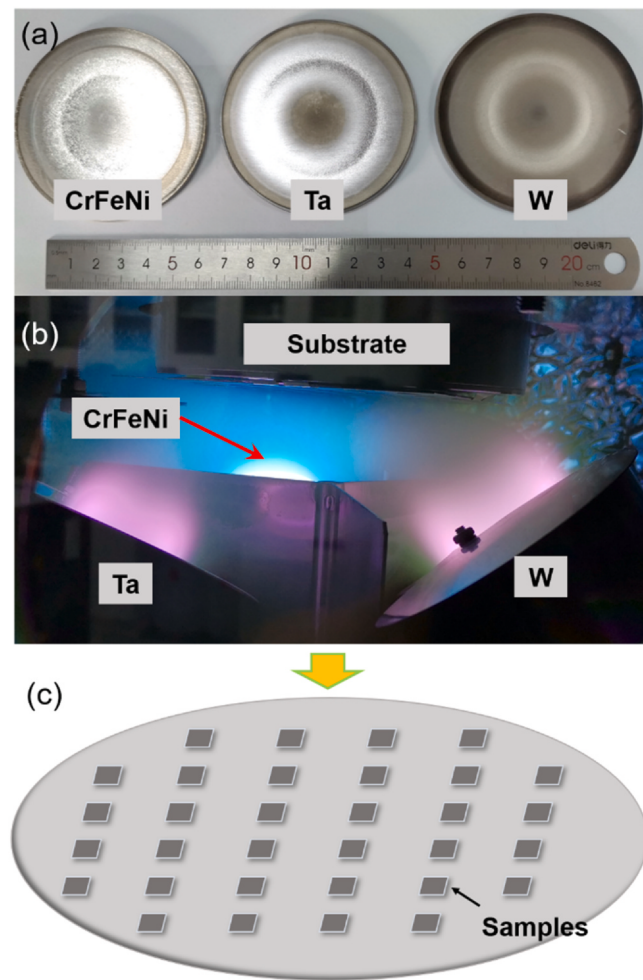


**Fig. 1.** (a) The alloy targets for magnetron sputtering, (b) the magnetron-sputtering process, and (c) the W-Ta-CrFeNi pseudo-ternary gradient film samples.

and a working distance of 13 mm, using the secondary electronic detector. The standard bright-field (BF), image, the selected area electron diffraction (SAED) patterns, and the line-scanning with the EDS were obtained by a transmission electron microscope (TEM, Tecnai F30) operated at 300 kV with EDS, and the TEM data processing adopts Digital Micrograph software. The TEM samples were taken from the surface to the substrate of the film as a thin foil with 100 nm thickness employing focused ion beam (FIB, Carl Zeiss Auriga, Germany) at 30 kV [49]. The crystalline structure of the sample was analyzed by a glancing incidence X-ray diffractometer (GIXRD, Bruker D8 Advance), with a Cu K $\alpha$  radiation and a scanning rate of 4°/min. The surface roughness of the film was measured by an atomic force microscope (AFM, Bruker Multimode 8) under a tapping mode with a scanning size of 500 nm, a scanning rate of 0.996 Hz, and a Bruker NCHV-A tips having a resonance frequencies ( $f_0$ ) of 320 kHz. The results were analyzed utilizing a Nano Scope Analysis software. The hardness of the sample was obtained, using a nanoindenter (MTS, Nano Indenter XP) and a Berkovich triangular pyramid indenter. The distance between each indentation on the film surface was 50 μm, continuous stiffness measurement. To avoid the effect of the substrate on hardness, the maximum displacement into the sample surface was 120–150 nm, 10 points were tested with each sample. The hardness and elastic modulus were averaged at 100–120 nm in depth.

### 3. Results

#### 3.1. Alloy design

The W and Ta are important parameters with high density and melting point in the fields of machining, engineering, and defense applications, such as high-speed steels. In addition, Cr, Fe, and Ni are the most widely used economic elements in the general high-entropy alloys with excellent properties. Numerous studies in recent years have demonstrated their excellent cost performance [50–52]. Therefore, these elements were selected to investigate the impact of entropy tuning on alloy properties. The atomic-radius difference ( $\delta$ ) vs. the mix-enthalpy ( $\Delta H_{mix}$ ) [53,54], and multi-component solid-solution rulers ( $\Omega$ ) [55] were employed to determine the phase structures of the alloy films. It is suggested that the alloy would form a solid-solution structure under the condition of  $-20 \text{ kJ}\cdot\text{mol}^{-1} \leq \Delta H_{mix} \leq 5 \text{ kJ}\cdot\text{mol}^{-1}$ ,  $\Omega \geq 1.1$ , and  $\delta \leq 6.6\%$ . Furthermore, the valence electron concentration (VEC) [56] could determine the face-centered-cubic or BCC structure of the alloy. When  $\text{VEC} \geq 8.0$ , a face-centered-cubic (FCC) phase could be obtained. When  $\text{VEC} < 6.87$ , a BCC phase could form. The parameters are defined as follows:

$$\delta = 100 \sqrt{\sum_{i=1}^n c_i \left(1 - \frac{r_i}{\sum_{i=1}^n c_i r_i}\right)^2} \quad (1)$$

$$\Delta H_{mix} = \sum_{i=1, i \neq j}^n 4c_i c_j \Delta H_{mix}^{ij} \quad (2)$$

$$\Delta S_{mix} = -R \sum_i^n c_i \ln c_i \quad (3)$$

$$\Omega = |T_m \Delta S_{mix}/\Delta H_{mix}| \quad (4)$$

$$\text{VEC} = \sum_1^n c_i (\text{VEC})_i \quad (5)$$

where  $c_i$  and  $c_j$  are the molar contents of the  $i$ th and  $j$ th components, respectively. The  $r_i$  is the atomic-radius size, and  $T_m$  is the theoretical melting point.

**Table 1** lists the basic physical constants of the alloying elements. The calculated results indicated that WTaCrFeNi with an equal atomic ratio had a  $\Delta H_{mix}$  of  $-11.20 \text{ kJ}\cdot\text{mol}^{-1}$ ,  $\delta$  of  $5.93\%$ ,  $\Omega$  of  $3.02$ , and VEC of  $7$ . It was found that the alloy could form FCC or BCC solid-solution structure, according to the scope of the above design guidelines.

#### 3.2. The composition and phase structure of the gradient thin films

The composition at the center of 32 thin-film samples could reflect the changes in the constituents of the gradient sample. As can be seen from **Table 1**, the high-throughput preparation could be applied to alloy samples with large compositions. Since the sample is an island design, the composition of each sample varied widely. The three target W-Ta-CrFeNi was composed of a W element (2.47 at% ~ 81.19 at%), Ta element (3.61 at% ~ 89.97 at%), and CrFeNi (1 at.% ~ 30 at%). In addition, the gradient thin-film samples had a large compositional range in the central region and smaller regions near the targets, as shown in **Fig. 2**. The composition region of these samples covered the phase-diagram boundary region to the central

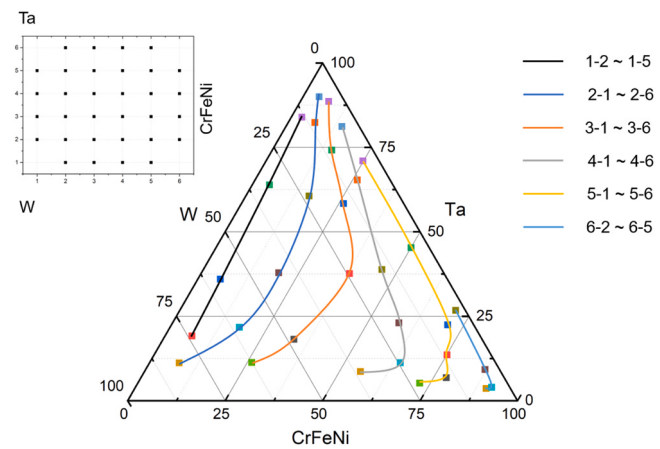


**Fig. 2.** The location diagram and the composition point by EDS of the 32 W-Ta-CrFeNi system gradient film samples.

**Table 2**  
The compositions of the W-Ta-CrFeNi gradient thin films.

Composition ( at% )	Position of the samples	1	2	3	4	5	6
W	1	—	73.91	58.24	31.68	13.33	—
Ta	—	—	19.15	35.99	63.87	83.93	—
Cr	—	1.9	1.6	1.32	0.86	—	—
Fe	—	2.45	2.09	1.36	1.23	—	—
Ni	—	2.58	2.08	1.78	0.65	—	—
W	2	81.19	60.5	42.3	23.13	10.8	5.92
Ta	—	11.18	21.72	37.88	60.64	82.33	89.97
Cr	—	2.32	5.98	5.7	4.87	1.66	1.24
Fe	—	2.43	6.01	6.34	4.9	2.64	1.31
Ni	—	2.88	5.79	7.78	6.46	2.57	1.56
W	3	62.55	48.26	24.27	15.45	10.56	4.08
Ta	—	11.27	18.19	37.62	58.35	74.21	88.63
Cr	—	8.38	10.75	12.21	8.76	4.13	2.55
Fe	—	9.06	11.09	12.95	7.45	4.33	2.34
Ni	—	8.74	11.71	12.95	9.99	6.77	2.39
W	4	35.97	24.42	18.91	15.39	8.42	4.48
Ta	—	8.62	11.24	23	38.81	65.37	81.15
Cr	—	17.49	20.46	18.47	14.58	7.23	4.76
Fe	—	19.31	22.49	20.55	15.45	9.55	4.25
Ni	—	18.62	21.38	19.07	15.78	9.43	5.35
W	5	22.49	14.87	11.3	6.71	4.65	4.18
Ta	—	5.19	6.81	13.53	22.44	45.31	70.99
Cr	—	23.94	26.09	24.27	22.84	15.37	6.7
Fe	—	25.05	27.87	26.76	24.04	16.67	8.24
Ni	—	23.34	24.36	24.15	23.97	18	9.89
W	6	—	6.25	4.67	3.69	2.47	—
Ta	—	—	3.61	3.96	9.24	26.74	—
Cr	—	—	29.64	30.08	28.17	22.93	—
Fe	—	—	32.56	32	30.03	23.56	—
Ni	—	—	27.94	29.28	28.87	24.29	—

region, which clearly showed the change of the sample composition. **Table 2** lists the compositions of the gradient films obtained from the EDS analysis.

**Fig. 3(a)** displays the relationship between the statistical XRD and composition results of the gradient films, which was plotted using an OriginLab™ ternary contour line with a smoothing parameter of 0.05. These thin films could form a nano-BCC and metallic glasses (MG) structure. The dual-phase structure (BCC1 + BCC2) was formed in the region near the W or Ta target as low-entropy alloy films which the composition at the boundary and corners of the pseudo-ternary diagram. The single-phase BCC structure was generated in the regions near the W and Ta targets and away from the CrFeNi target. The nanocrystalline and MG structure coexist in the center region of the phase diagram. The region near the CrFeNi target is a MG area. Due to a higher deposition rate of W and Ta, the films near

**Table 1**

The basic physical constants of alloying elements.

Element	Cr	Fe	Ni	Ta	W
r (Å)	1.25	1.24	1.25	1.43	1.37
$\rho$ (g/cm³)	7.19	7.85	8.90	16.65	19.35
Crystal structure	BCC	FCC/BCC	FCC	BCC	BCC
VEC	6	8	10	5	6
$T_m$ (K)	2130	1811	1726	3269	3683

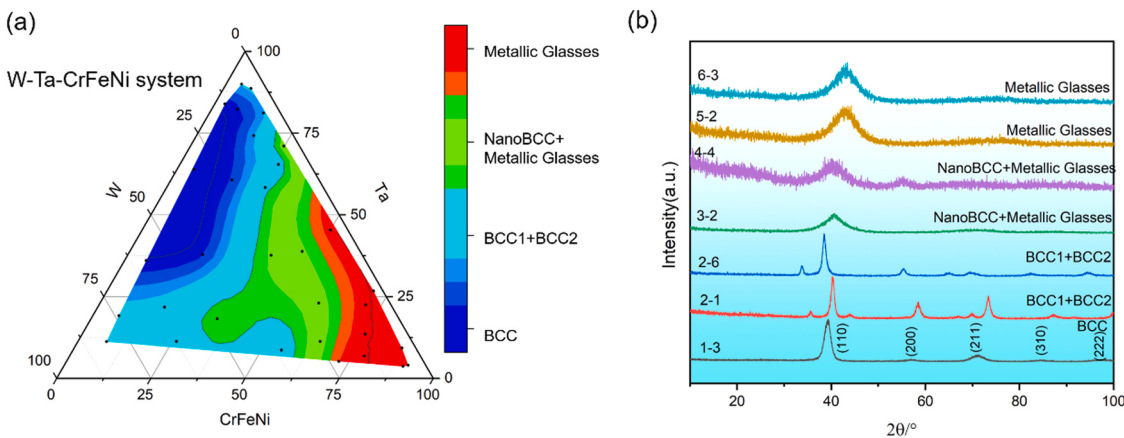


**Fig. 3.** The phase structure of the W-Ta-CrFeNi system by XRD data, (a) the relationship between the composition and the phase structure, the black spots in the figures are the composition data, (b) the XRD pattern of some typical film samples.

the W and Ta targets are thicker than that near the CrFeNi target. This trend may explain why the films formed a BCC structure near the W and Ta targets and metallic glass near the CrFeNi target. The rapid deposition of magnetron sputtering is mainly attributed to the formation of an amorphous structure in these alloys. Fig. 3(b) shows the XRD patterns of typical film samples, which accurately represented the change of the phase structure in gradient thin films from the nano-BCC structure to the amorphous structure.

### 3.3. The microstructures of the thin films

Fig. 4 presents the surface microstructures of these thin films. It can be seen that the microstructure of the film surface varies with changing the composition. With a higher content of W or Ta, the surface microstructures of the samples would exhibit a needle-like morphology, as demonstrated in Fig. 4(b) and (c). As the W and Ta contents in the alloy film increased, the surface morphologies of these films exhibit circular drums, as presented in Fig. 4(a). When the film composition is in the high-entropy region, the surface showed a smooth surface and nano-drum-capped topography, as shown in Fig. 4(d). When the film composition is located on the

CrFeNi side, the alloy-film surface exhibited a smooth surface morphology accompanied by a large number of nano-cracks, as shown in Fig. 4(e) and (f). Meanwhile, the cross-sectional SEM micrograph of the thin films in Fig. 4 displayed that the film thickness is greater near the W or Ta target, while smaller near the rich CrFeNi region. The thickness values of these films are shown in the Fig. 4, 853.2, 875.3, 975.7, 637.6, 582.2, and 613.1 nm, respectively.

The cross-section near the W or Ta target presented a columnar structure, which became smooth with the increase of the CrFeNi. These films rich with W or Ta show nano-needles with the surface morphology, the columnar structure of the cross-section exhibits a small needle shape, and the size of the cross-section columnar structure is minimized, which is shown inset of Fig. 4 (b) and (c). The films rich in W and Ta show the nano-drums in the surface morphology. The columnar structure of the cross-section exhibits a cylindrical shape. The size of columnar structure of the cross-section was the largest, exhibited inset of Fig. 4 (a) and (e). The films rich in the CrFeNi present an MG phase structure. The columnar structure of the cross section exhibits cleavage. The size of the columnar structure of the cross-section was uncertain, shown inset of Fig. 4 (e) and (f).

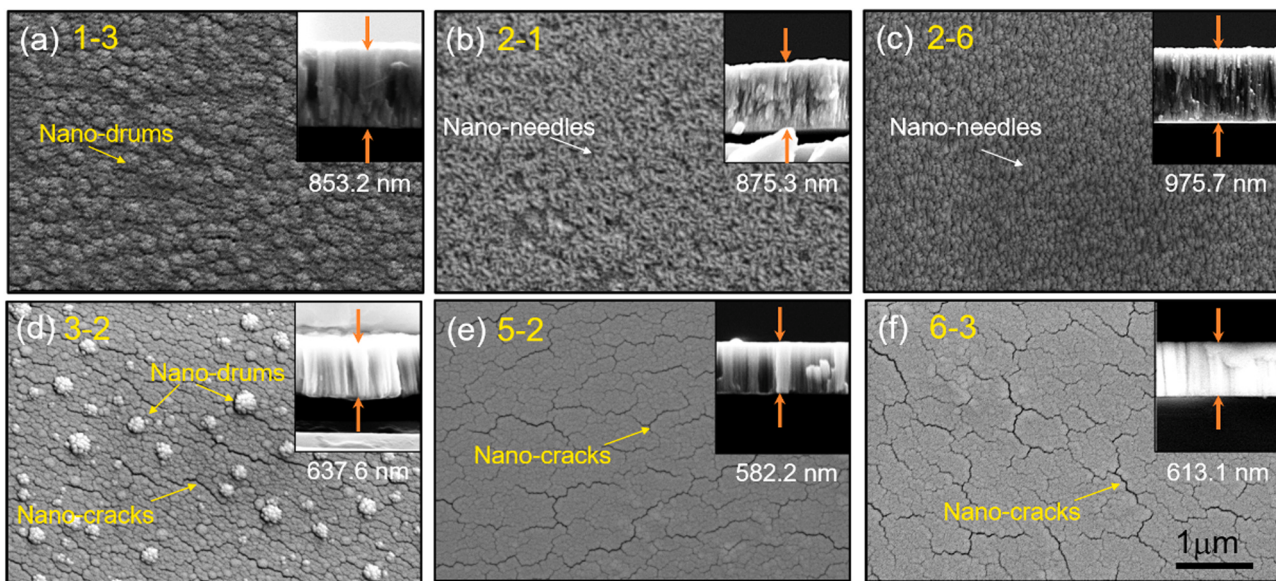


**Fig. 4.** The SEM photos of the surfaces and cross-section microstructures of the films, (a) the  $W_{58.24}Ta_{35.99}Cr_{1.6}Fe_{2.09}Ni_{2.08}$ , (b) the  $W_{8.19}Ta_{11.18}Cr_{2.32}Fe_{2.43}Ni_{2.88}$ , (c) the  $W_{5.92}Ta_{89.97}Cr_{1.24}Fe_{1.31}Ni_{1.56}$ , (d) the  $W_{24.27}Ta_{37.62}Cr_{12.21}Fe_{12.95}Ni_{12.95}$ , (e) the  $W_{14.87}Ta_{6.81}Cr_{26.09}Fe_{27.87}Ni_{24.36}$ , and (f) the  $W_{4.67}Ta_{3.96}Cr_{30.08}Fe_{32}Ni_{29.28}$ , the scale bar is the same in the figures shown in Figure (f).

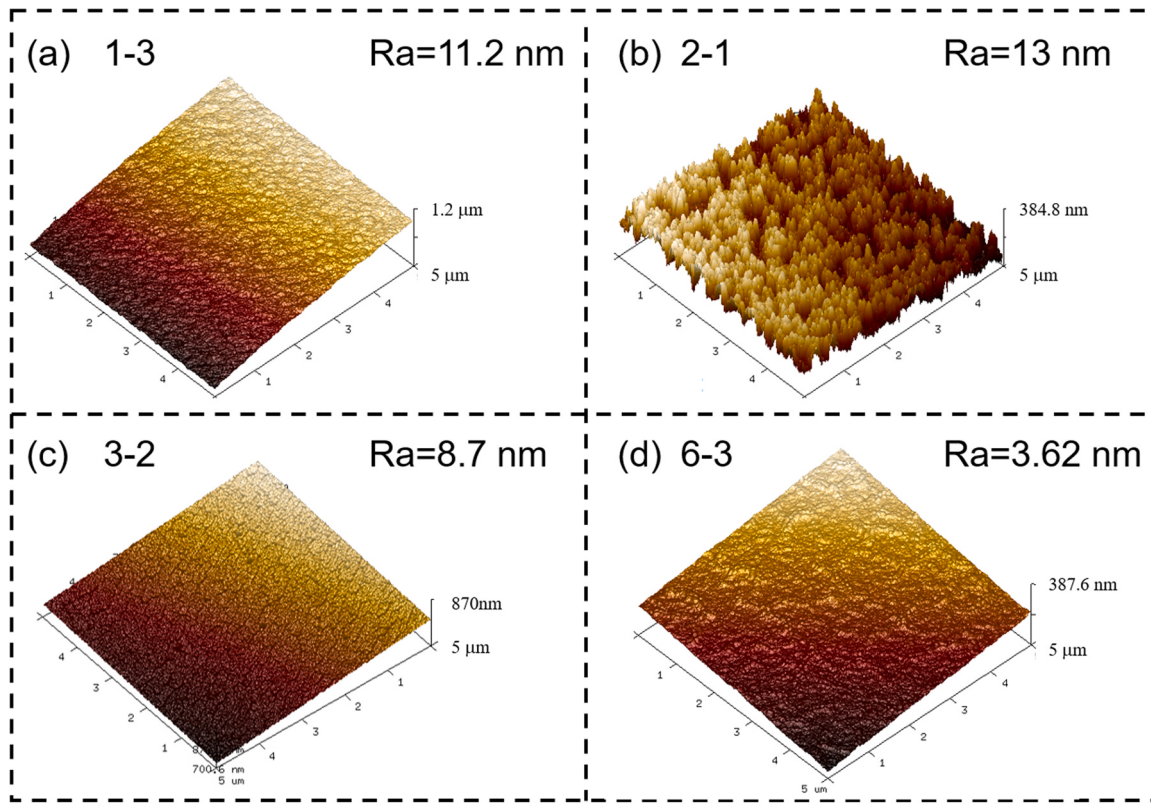


**Fig. 5.** The AFM pictures of some gradient film surfaces with different roughness.

**Fig. 5** shows AFM images of the W-Ta-CrFeNi gradient film samples. It can be seen that the samples near the W or Ta target displayed a rougher surface than those near the CrFeNi target. The surface roughness of Samples 1-3 and 2-1 reached more than ~10 nm, while the samples at the center of the phase diagram had a lower roughness with ~8.7 nm for Sample 3-3. Sample 6-3 near the CrFeNi target displayed the lowest roughness of ~3.62 nm, which agreed with the results of SEM measurements. Furthermore, the surface of the gradient film reached a certain angle between the substrates. Moreover, the angle was larger at the center of the phase diagram, probably due to the difference in elemental sputtering rates of multiple target co-sputtering.

### 3.4. Properties

**Fig. 6** shows the nanoindentation hardness and elastic modulus (G) of these thin films. The nanoindentation and the composition were plotted, using the OriginLab<sup>TM</sup> ternary contour line with a smoothing parameter of 0.05. As shown in **Fig. 6(a)**, the nanoindentation hardness of the thin films had a maximum value of ~20.6 GPa and a minimum value of ~9.9 GPa. Overall, the alloy film exhibits excellent hardness. It shows that the alloy system has potential applications in the field of ultra-hard alloys. At the same time, there is a nonlinear relationship between the hardness and mix-entropy of these alloy films. The region near the W and Ta targets exhibited a higher hardness than that at the center of the three-dimensional diagram region. The W<sub>15.39</sub>Ta<sub>38.81</sub>Cr<sub>14.58</sub>Fe<sub>15.45</sub>Ni<sub>15.77</sub> alloy near the center region displayed the highest hardness. **Table 3** lists the hardness of the gradient thin films. In addition, **Fig. 6(b)** displays the modulus of the alloy gradient films. The results indicated that there was an elastic modulus low valley region at the center of the pseudo-ternary diagram, and a higher elastic modulus region in the W-rich region. **Table 4** lists the elastic modulus of the gradient thin films.

As the size of the columnar structure with the films rich in whether W or Ta is smaller than that of the films rich in both W and Ta shown inset of **Fig. 4** (a), (b), and (c), therefore, the hardness of the alloy film close to the W or Ta target is higher than the films rich in W and Ta. The composition of the alloy films is in the region near the W and Ta in the center of the pseudo-ternary phase diagram. The surface morphology presents an isolated nano-drum, which is in the transition zone of the phase structure, the crystalline to the MG phase structure, shown with inset of **Fig. 4** (d). In addition, the cross-section of the MG region exhibits typical shear fracture characteristics. The sizes of the columnar structures of the cross-sections with these samples are irregularly presented inset of **Fig. 4**(e) and (f). Therefore, the effect on the properties with the columnar structure is not obvious on the samples contain MG structure.

## 4. Discussion

### 4.1. The phase formation of the W-Ta-CrFeNi alloy system films

The  $\Omega - \delta$  of the W-Ta-CrFeNi system films was calculated and exhibited in **Fig. 7(a)**. **Fig. 7(b)** shows the  $\Omega - \delta$  of the W-Ta-CrFeNi system films, compared to the other alloys. It can be seen that the  $\Omega - \delta$  of these alloys just filled the solid solution and intermetallics (SS + I) region, above the MG region [54,55]. The  $\Omega$  in the Briggs logarithm ( $\lg$ ) coordinate system indicated that these alloys formed the MG structure and were located below the solid-solution region in the pattern of the  $\Omega - \delta$ . When the alloy had the same  $\delta$ , the higher the  $\Omega$ , the easier it is for the alloy to form a solid-solution structure. The  $\lg\Omega - \delta$  data and the MG of the solid solutions formed by different compositions were linearly fitted by the Origin software, and the results were presented with Formulas (6) and (7), respectively.

$$\lg(\Omega) = -0.108 * \delta + 1.305 \quad (6)$$

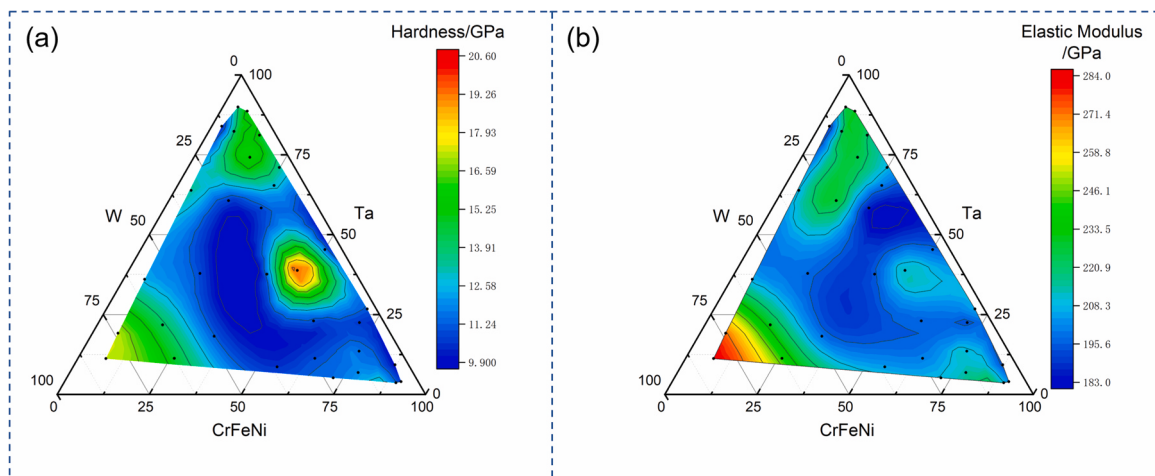


**Fig. 6.** The (a) and (b) are the hardness and the elastic modulus vs. the composition data of W-Ta-CrFeNi gradient thin films, the black spots in the figures are the composition data.

**Table 3**

The hardness of the W-Ta-CrFeNi gradient films by nanoindentation tests.

Hardness/GPa						
Position	1	2	3	4	5	6
1	–	17.2	12.4	13.4	10.2	–
2	17.3	14.1	11.0	10.5	14.5	13.8
3	14.8	11.1	10.9	10.9	16.3	15.7
4	10.5	11.1	10.6	20.6	12.9	14.7
5	11.5	11.8	11.9	10.6	11.3	13.4
6	–	12.3	10.5	9.9	11.2	–

**Table 4**

The elastic modulus of the W-Ta-CrFeNi gradient films by nanoindentation tests.

Elastic modulus / GPa						
Position	1	2	3	4	5	6
1	–	272.9	206.3	208.2	188.3	–
2	283.7	229.6	197.3	229.6	229.1	226.6
3	241.7	198.3	193.7	183.3	226.1	229.7
4	204.7	200.6	196.3	214.5	200.0	219.4
5	208.7	211.9	214	193.3	196.5	208.1
6	–	218.5	200.6	193.4	205.8	–

$$\lg(\Omega) = -0.126 * \delta + 1.221 \quad (7)$$

The goodness of fit ( $R^2$ ) of these two linear fit lines are 0.755 and 0.655, respectively. The absolute value of the slope of the straight line in the MG region is larger than that of the solid-solution region, with a smaller intercept. The composition with a higher  $\Omega$  is more likely to form the solid-solution structure than the MG structure under the same  $\delta$  value.

Therefore, for the W-Ta-CrFeNi system magnetron-sputtering film samples, the MG region expanded in the  $\Omega - \delta$  phase-formation criterion. There is a rapidly-quenched process during the formation of the thin films. Therefore, the alloys possessed a large degree of under cooling during the thin-film preparation. In addition, the current melting point ( $T_{current}$ ) of the alloy film is lower than the theoretical melting point ( $T_m$ ), as presented in Eqs. (8) and (9).

$$T_{current} = T_m - \Delta T \quad (8)$$

$$\Omega_{films} = |T_{current} \Delta S_{mix}/\Delta H_{mix}| \quad (9)$$

where  $\Delta T$  is the degree of under cooling [57]. Therefore, the current  $\Omega$  required for the alloy films to form the MG structure was lower than that of the bulk alloy. Since the melting points of the W and Ta are higher than those of the Cr, Fe, and Ni, the  $\Delta T$  of the composition rich in the W and Ta was less affected by the  $T_m$ . Finally, the alloy films with the W and Ta enriched alloy films formed a solid-solution

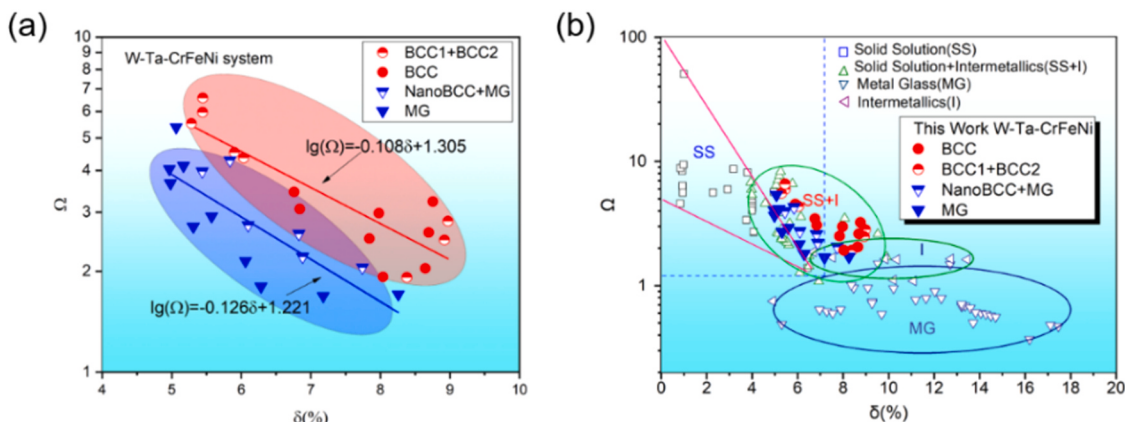


**Fig. 7.** (a) The  $\Omega - \delta$  phase formation criterion of the W-Ta-CrFeNi system films, (b) the  $\Omega - \delta$  phase formation criterion of the W-Ta-CrFeNi system films compared with other alloys.

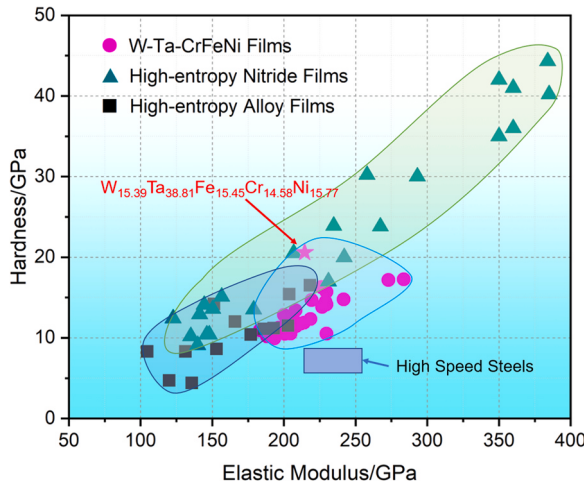


**Fig. 8.** The hardness vs. the elastic modulus with different compositions of the high-entropy alloy films, the high-entropy nitride films, and the W-Ta-CrFeNi system alloy films.

structure, and the Cr, Fe, and Ni-enriched alloy films formed a MG structure, as shown in Fig. 3(a).

#### 4.2. The hardness and the modulus with different compositions

According to the screening of the gradient film composition, it was found that the highest hardness of the  $W_{15.39}Ta_{38.81}Cr_{14.58}Fe_{15.45}Ni_{15.77}$  high-entropy film reached  $\sim 20.6$  GPa, which was higher than most high-entropy alloy films, and even comparable to some high-entropy nitride material films [17,31,46–48,58], as exhibited in Fig. 8. Similarly, the hardness and modulus of these alloy films were between those of the high-entropy alloy films and the high-entropy nitride material films, providing a novel material composition database for the development of advanced ultra-hard materials. Furthermore, some studies found that the high-entropy high entropy oxides (HEO) [48] and high-entropy carbide [59–62] present excellent properties. We believe that the developed nitride, oxide, or carbide film can further enhance the properties of this type alloy thin films.

Fig. 9(a) shows the XRD pattern of the  $W_{15.39}Ta_{38.81}Cr_{14.58}Fe_{15.45}Ni_{15.77}$  high-entropy films. It can be seen that these alloy films exhibited the main phase with an MG structure, and as the main peak in the XRD pattern is sharp and there is a

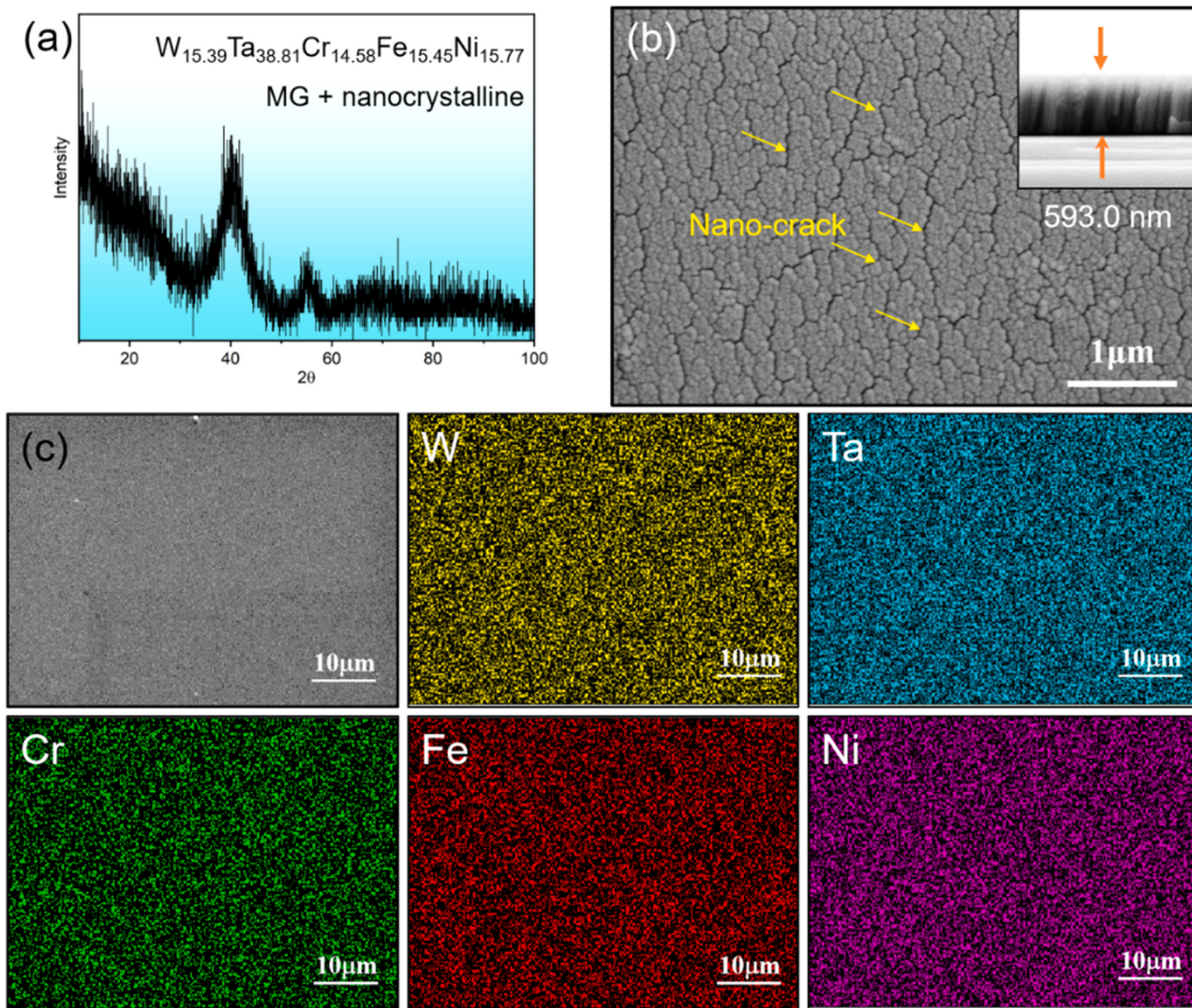


**Fig. 9.** The XRD pattern, the microstructure, and the EDS mapping of the  $W_{15.39}Ta_{38.81}Cr_{14.58}Fe_{15.45}Ni_{15.77}$  high-entropy alloy film, (a) the XRD pattern, (b) the surface microstructure and with the illustration of cross-section, and (c) the EDS mapping.

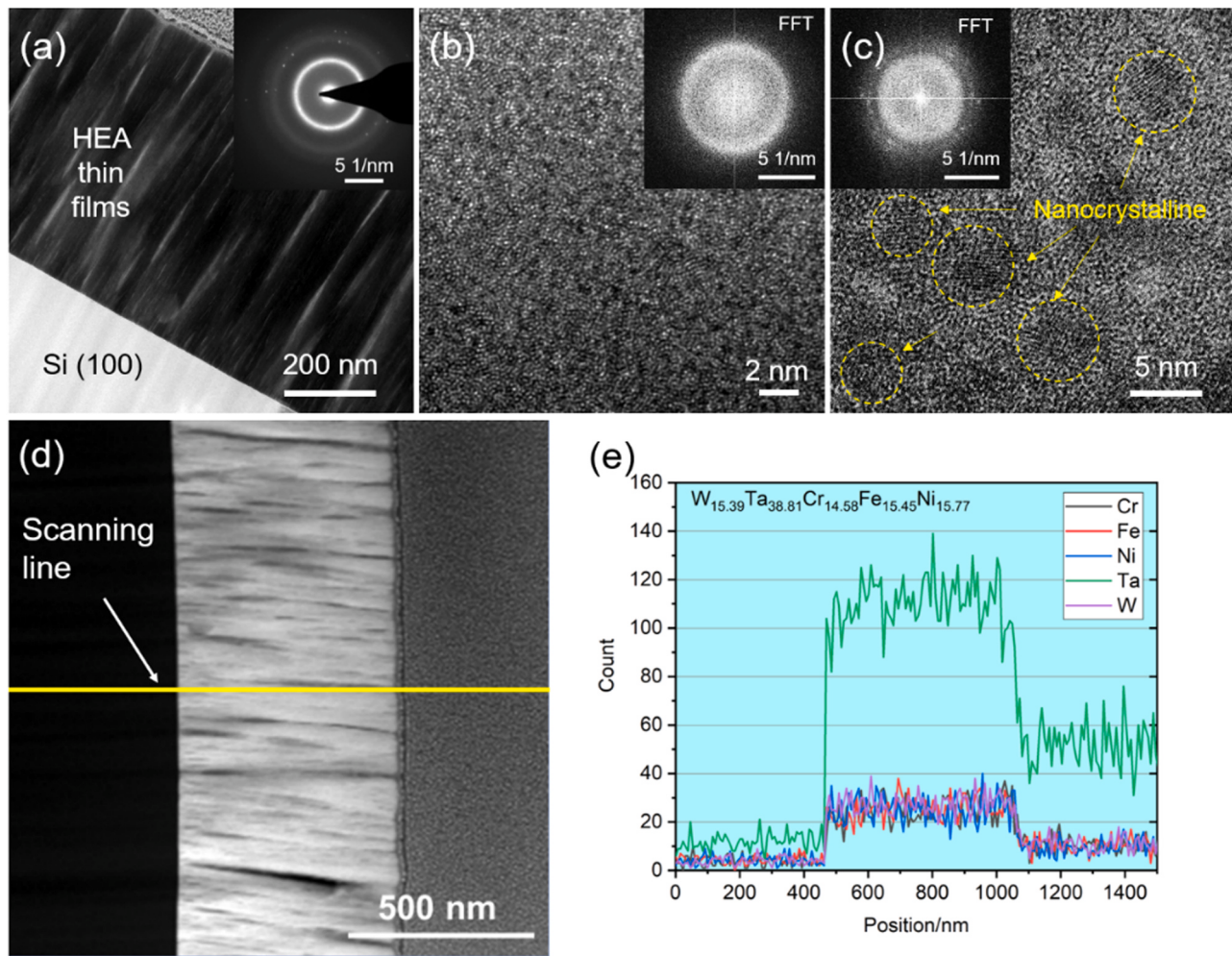


**Fig. 10.** Cross-sectional TEM images of the  $\text{W}_{15.39}\text{Ta}_{38.81}\text{Cr}_{14.58}\text{Fe}_{15.45}\text{Ni}_{15.77}$  high-entropy alloy thin film. (a) the BF image with the illustration of SAED images (b), the high-resolution images with the illustration of the FFT images, (c) HAADF-STEM and the illustration of the FFT images, (d) STEM image with scanning line, (e) the result of the EDS line scanning.

peak at  $55.5^\circ$ , this feature indicated that there are some nanocrystalline structures appearing in the films. As can be seen from Fig. 9(b), the  $\text{W}_{15.39}\text{Ta}_{38.81}\text{Cr}_{14.58}\text{Fe}_{15.45}\text{Ni}_{15.77}$  high-entropy alloy film displayed a smooth surface with some nano-cracks, with a thickness of 593.0 nm, similar to Fig. 4(e). The EDS mapping results, as shown in Fig. 9(c), indicated that the elements had a uniform distribution.

Fig. 10(a) shows the TEM bright-field image of the cross-section of the  $\text{W}_{15.39}\text{Ta}_{38.81}\text{Cr}_{14.58}\text{Fe}_{15.45}\text{Ni}_{15.77}$  high-entropy alloy thin film. It can be seen from the figure that the alloy film grows in a columnar shape along the direction of the substrate. Fig. 10 (a)(inset) is the selected area electron diffraction (SEAD) pictures of the thin films, presenting that the phase structures of this film are the MG and some nanocrystalline phases. Fig. 10(b) and (c) are high-resolution pictures with the MG phase arear near the Si substrate and high-angle annular dark field (HAADF) scanning transmission electron microscopy (STEM) with the illustration of fast Fourier transform (FFT) images near the surface of the film, respectively. They all show that the main phase of the thin film is the amorphous structure, and some nanocrystalline structure appears near the surface of the film. This finding is consistent with the XRD results shown in Fig. 9 (a). Fig. 10 (d) and (e) are STEM images and EDS line scan pictures of the alloy films along the growth direction. The composition of the film is uniform along the growth direction.

The highest hardness could be attributed to the nano-grain and the MG structure. In addition, Wu et al. [63] present a new strategy

to investigate the Cr-Co-Ni (crystalline)/Ti-Zr-Nb Hf-Cr-Co-Ni (amorphous) laminate composite alloy, which had realized the preparation of thermally stable, ultra-strong and deformable crystal-glass nanocomposites. Since the atomic sizes of the W and Ta are different from those of the Cr, Fe, and Ni, the large lattice distortion formed in this alloy film could enhance the strengthen of the solid solution, leading to an increased hardness of the alloy film. Therefore, the combination of three strengthening mechanisms of strong solid solution + nanocrystalline-phase strengthening + amorphous phase ternary composite strengthening may result in an ultra-high nanoindentation hardness of the alloy film.

#### 4.3. The influence of the entropy ( $S$ ) and the modulus

The alloy element, W, showed a high elastic modulus. Hence, a high modulus region was generated near the W target. In addition, the alloys have a lower modulus with high mix entropy. The thermodynamics equation among the entropy,  $S$ , internal energy,  $U$ , and volume modulus,  $K$  is defined as follows.

$$K = V \left( \frac{\partial^2 U}{\partial V^2} \right)_T - VT \left( \frac{\partial^2 S}{\partial V^2} \right) \quad (10)$$

where the  $V$  is the volume, and  $T$  is the thermodynamic temperature. According to the previous study of Raju [64], the relationship could be simplified as follows.

$$K_s \approx -T\alpha_V K \quad (11)$$

where the  $K_s$  is the volume modulus, given by the  $S$ . The  $\alpha_V$  is the volume-expansion coefficient. It was revealed that the larger entropy value of the alloy, the smaller the volume modulus. Furthermore, the elastic modulus,  $G$ , was related to the volume modulus, as shown below.

$$K = \frac{2}{3}G + \lambda \quad (12)$$

where the  $\lambda$  is the Lamé constant. The trend suggested that the elastic modulus,  $G$ , and volume modulus,  $K$ , were positively correlated. That is, a larger  $K$  means a higher  $G$ . Therefore, a negative correlation also existed between the entropy,  $S$ , and elastic modulus,  $G$ , which could explain why a low elastic modulus region appeared at the center of the ternary diagram and near the CrFeNi target region with high entropy. Therefore, there was a correspondence between the high entropy and low elastic modulus. Similar phenomena had been previously reported by Yan et al. [16].

## 5. Conclusions

In the present work, the W-Ta-CrFeNi gradient-alloy films were successfully fabricated by the three-target magnetron co-sputtering method. The composition coverage of alloy films is  $\sim 1.00$  at% to a central region of a maximum of  $\sim 89.97$  at%, basically covering all alloy compositions. A large degree of under cooling existed in the magnetron-sputtering method, which has a negative impact on the  $\Omega$ , and expanded the MG region in the  $\Omega - \delta$  phase formation rule. There is a nonlinear relationship between the hardness and the entropy. The  $W_{15.39}Ta_{38.81}Cr_{14.58}Fe_{15.45}Ni_{15.77}$  alloy film shows the maximum hardness of  $\sim 20.6$  GPa. The strong solid-solution strengthening, nanocrystalline strengthening and metallic glasses strengthening may be attributed to the ultra-high hardness of the alloy. The film with the high-entropy composition exhibited a low modulus, indicating a negative correlation between the entropy,  $S$ , and elastic modulus,  $G$ . Based on this approach, the rapid screening of the W-Ta-CrFeNi high-entropy alloys could be realized to provide a material database for developing novel alloy materials.

## CRediT authorship contribution statement

**Yasong Li:** Conceptualization, Formal analysis, Investigation, Methodology, Validation, Visualization, Writing – original draft. **Jiang Ma:** Methodology, Resources, Writing-review. **Peter K. Liaw:** Investigation, Validation, Writing-review, Funding acquisition. **Yong Zhang:** Investigation, Validation, Resources, Conceptualization, Writing – review & editing, Supervision, Funding acquisition.

## Declaration of Competing Interest

The authors declare that they have no known competing financial interests or personal relationships that could have appeared to influence the work reported in this paper.

## Acknowledgements

The present work was supported by the Guangdong Basic and Applied Basic Research Foundation (2019B1515120020), the State Key Laboratory for Advanced Metals and Materials at the University of Science and Technology Beijing (2020-Z08), the Funds for Creative Research Groups of China (No. 51921001), and National Natural Science Foundation of China (No. 51671020); P. K. Liaw appreciates the support from the National Science Foundation (DMR-1611180 and 1809640) and the US Army Research Office (W911NF-13-1-0438

and W911NF-19-2-0049). Yasong Li would like to thank Xuehui Yan, Ruixuan Li, and Qiuwei Xing for their help with this article.

## References

- [1] J.W. Yeh, S.K. Chen, S.J. Lin, J.Y. Gan, T.S. Chin, T.T. Shun, C.H. Tsau, S.Y. Chang, Nanostructured high-entropy alloys with multiple principal elements: novel alloy design concepts and outcomes, *Adv. Eng. Mater.* 6 (2004) 299–303.
- [2] Y. Zhang, T.T. Zuo, Z. Tang, M.C. Gao, K.A. Dahmen, P.K. Liaw, Z.P. Lu, Microstructures and properties of high-entropy alloys, *Prog. Mater. Sci.* 61 (2014) 1–93.
- [3] W. Zhang, P.K. Liaw, Y. Zhang, Science and technology in high-entropy alloys, *Sci. China Mater.* 61 (2018) 2–22.
- [4] P. Shi, R. Li, Y. Li, Y. Wen, W. Ren, Z. Shen, T. Zheng, J. Peng, X. Liang, P. Hu, N. Min, Y. Zhang, Y. Ren, P.K. Liaw, D. Raabe, Y. Wang, Hierarchical crack buffering triples ductility in eutectic herringbone high-entropy alloys, *Science* 373 (2021) 912–918.
- [5] Q. Pan, L. Zhang, R. Feng, Q. Lu, K. An, A.C. Chuang, J.D. Poplawsky, P.K. Liaw, L. Lu, Gradient cell-structured high-entropy alloy with exceptional strength and ductility, *Science* 374 (2021) 984–989.
- [6] M. Vaidya, G.M. Muralikrishna, B.S. Murty, High-entropy alloys by mechanical alloying: a review, *J. Mater. Res.* 34 (2019) 664–686.
- [7] N. Xu, Z. Yang, X. Mu, Y. Huang, S. Li, Y. Wang, Effect of Al addition on the microstructures and deformation behaviors of non-equiautomatic FeMnCoCr metastable high entropy alloys, *Appl. Phys. Lett.* 119 (2021) 261902.
- [8] Y. Wu, P.K. Liaw, Y. Zhang, Preparation of bulk TiZrNbMoV and NbTiAlTaV high-entropy alloys by powder sintering, *Metals* 11 (2021) 1748.
- [9] E.P. George, D. Raabe, R.O. Ritchie, High-entropy alloys, *Nat. Rev. Mater.* 4 (2019) 515–534.
- [10] G. Karthick, L. Raman, B.S. Murty, Phase evolution and mechanical properties of novel nanocrystalline  $Y_2(TiZrHfMoV)_2O_7$  high entropy pyrochlore, *J. Mater. Sci. Technol.* 82 (2021) 214–226.
- [11] Y. Li, P.K. Liaw, Y. Zhang, Microstructures and properties of the low-density  $Al_{15}Zr_{40}Ti_{28}Nb_{12}M(Cr, Mo, Si)_5$  high-entropy alloys, *Metals* 12 (2022) 496.
- [12] L. Li, M. Li, M. Liu, B. Sun, C. Wang, J. Huo, W. Wang, Y. Liu, Enhanced oxidation resistance of MoTaTiCrAl high entropy alloys by removal of Al, *Sci. China Mater.* 64 (2021) 223–231.
- [13] R. Potyrailo, K. Rajan, K. Stoeve, I. Takeuchi, B. Chisholm, H. Lam, Combinatorial and high-throughput screening of materials libraries: review of state of the art, *ACS Comb. Sci.* 13 (2011) 579–633.
- [14] Y. Zhang, X. Yan, J. Ma, Z. Lu, Y. Zhao, Compositional gradient films constructed by sputtering in a multicomponent Ti-Al-(Cr, Fe, Ni) system, *J. Mater. Res.* 33 (2018) 3330–3338.
- [15] Q. Xing, J. Ma, C. Wang, Y. Zhang, High-throughput screening solar-thermal conversion films in a pseudobinary (Cr, Fe, V)-(Ta, W) system, *ACS Comb. Sci.* 20 (2018) 602–610.
- [16] X. Yan, J. Ma, Y. Zhang, High-throughput screening for biomedical applications in a Ti-Zr-Nb alloy system through masking co-sputtering, *Sci. China Phys. Mech.* 62 (2019) 996111.
- [17] X.H. Yan, J.S. Li, W.R. Zhang, Y. Zhang, A brief review of high-entropy films, *Mater. Chem. Phys.* 210 (2018) 12–19.
- [18] R. Li, Z. Wang, Z. Guo, P.K. Liaw, T. Zhang, L. Li, Y. Zhang, Graded microstructures of Al-Li-Mg-Zn-Cu entropic alloys under supergravity, *Sci. China Mater.* 62 (2019) 736–744.
- [19] R.X. Li, P.K. Liaw, Y. Zhang, Synthesis of Al<sub>x</sub>CoCrFeNi high-entropy alloys by high-gravity combustion from oxides, *Mater. Sci. Eng. A* 707 (2017) 668–673.
- [20] L. Zhao, L. Jiang, L.X. Yang, H. Wang, W.Y. Zhang, G.Y. Ji, X. Zhou, W.A. Curtin, X.B. Chen, P.K. Liaw, S.Y. Chen, H.Z. Wang, High throughput synthesis enabled exploration of CoCrFeNi-based high entropy alloys, *J. Mater. Sci. Technol.* 110 (2022) 269–282.
- [21] J.W. Pegues, M.A. Melia, R. Puckett, S.R. Whetten, N. Argibay, A.B. Kustas, Exploring additive manufacturing as a high-throughput screening tool for multiphase high entropy alloys, *Addit. Manuf.* 37 (2021) 101598.
- [22] C. Haase, F. Tang, M.B. Wilms, A. Weisheit, B. Hallstedt, Combining thermodynamic modeling and 3D printing of elemental powder blends for high-throughput investigation of high-entropy alloys - towards rapid alloy screening and design, *Mater. Sci. Eng. A* 688 (2017) 180–189.
- [23] L. Zhao, Y. Zhou, H. Wang, X. Chen, L. Yang, L. Zhang, L. Jiang, Y. Jia, X. Chen, H. Wang, High-throughput synthesis and characterization of a combinatorial materials library in bulk alloys, *Metall. Mater. Trans. A* 52 (2021) 1159–1168.
- [24] L. Huang, J.M. Rondinelli, Reliable electrochemical phase diagrams of magnetic transition metals and related compounds from high-throughput ab initio calculations, *npj Mater. Degrav.* 3 (2019) 26.
- [25] S. Yang, J. Lu, F. Xing, L. Zhang, Y. Zhong, Revisit the VEC rule in high entropy alloys (HEAs) with high-throughput CALPHAD approach and its applications for material design-A case study with Al-Co-Cr-Fe-Ni system, *Acta Mater.* 192 (2020) 11–19.
- [26] R. Feng, C. Zhang, M.C. Gao, Z. Pei, F. Zhang, Y. Chen, D. Ma, K. An, J.D. Poplawsky, L. Ouyang, Y. Ren, J.A. Hawk, M. Widom, P.K. Liaw, High-throughput design of high-performance lightweight high-entropy alloys, *Nat. Commun.* 12 (2021) 4329.
- [27] Q. Xing, S. Xia, X. Yan, Y. Zhang, Mechanical properties and thermal stability of  $(NbTiAlSiZr)N_x$  high-entropy ceramic films at high temperatures, *J. Mater. Res.* 33 (2018) 3347–3354.

- [28] Y. Zhang, X.H. Yan, W.B. Liao, K. Zhao, Effects of nitrogen content on the structure and mechanical properties of  $(\text{Al}_{0.5}\text{CrFeNiTi}_{0.25})\text{N}_x$  high-entropy films by reactive sputtering, *Entropy* 20 (2018) 624.
- [29] N.A. Khan, B. Akhavan, C. Zhou, H. Zhou, L. Chang, Y. Wang, Y. Liu, L. Fu, M.M. Bilek, Z. Liu, RF magnetron sputtered  $\text{AlCoCrCu}_{0.5}\text{FeNi}$  high entropy alloy (HEA) thin films with tuned microstructure and chemical composition, *J. Alloy. Compd.* 836 (2020) 155348.
- [30] W.J. Sheng, X. Yang, J. Zhu, C. Wang, Y. Zhang, Amorphous phase stability of  $\text{NbTiAlSiN}_x$  high-entropy films, *Rare Met.* 37 (2018) 682–689.
- [31] W. Li, P. Liu, P. Liaw, Microstructures and properties of high-entropy alloy films and coatings: a review, *Mater. Res. Lett.* 6 (2018) 199–229.
- [32] C. Cheng, X. Zhang, M.J.R. Haché, Y. Zou, Magnetron co-sputtering synthesis and nanoindentation studies of nanocrystalline  $(\text{TiZrHf})_{x}(\text{NbTa})_{1-x}$  high-entropy alloy thin films, *Nano Res.* (2021).
- [33] N.A. Khan, B. Akhavan, H. Zhou, L. Chang, Y. Wang, L. Sun, M.M. Bilek, Z. Liu, High entropy alloy thin films of  $\text{AlCoCrCu}_{0.5}\text{FeNi}$  with controlled microstructure, *Appl. Surf. Sci.* 495 (2019) 143560.
- [34] H. Huang, P.K. Liaw, Y. Zhang, Structure design and property of multiple-basis-element (MBE) alloys flexible films, *Nano Res.* (2021), <https://doi.org/10.1007/s12274-021-3534-5>
- [35] X. Yan, Y. Zhang, A body-centered cubic  $\text{Zr}_{50}\text{Ti}_{35}\text{Nb}_{15}$  medium-entropy alloy with unique properties, *Scr. Mater.* 178 (2020) 329–333.
- [36] X. Yan, P.K. Liaw, Y. Zhang, Ultrastrong and ductile BCC high-entropy alloys with low-density via dislocation regulation and nanoprecipitates, *J. Mater. Sci. Technol.* 110 (2022) 109–116.
- [37] Q. Xing, J. Ma, Y. Zhang, Phase thermal stability and mechanical properties analyses of  $(\text{Cr},\text{Fe},\text{V}) - (\text{Ta},\text{W})$  multiple-based elemental system using a compositional gradient film, *Int. J. Min. Met. Mater.* 27 (2020) 1379–1387.
- [38] D.B. Miracle, O.N. Senkov, A critical review of high entropy alloys and related concepts, *Acta Mater.* 122 (2017) 448–511.
- [39] O.N. Senkov, G.B. Wilks, D.B. Miracle, C.P. Chuang, P.K. Liaw, Refractory high-entropy alloys, *Intermetallics* 18 (2010) 1758–1765.
- [40] O.N. Senkov, G.B. Wilks, J.M. Scott, D.B. Miracle, Mechanical properties of  $\text{Nb}_{25}\text{Mo}_{25}\text{Ta}_{25}\text{W}_{25}$  and  $\text{V}_{20}\text{Nb}_{20}\text{Mo}_{20}\text{Ta}_{20}\text{W}_{20}$  refractory high entropy alloys, *Intermetallics* 19 (2011) 698–706.
- [41] Y. Zou, H. Ma, R. Spolenak, Ultrastrong ductile and stable high-entropy alloys at small scales, *Nat. Commun.* 6 (2015) 7748.
- [42] W. Zhang, P. Liaw, Y. Zhang, A novel low-activation  $\text{VCrFeTa}_x\text{W}_x$  ( $x = 0.1, 0.2, 0.3, 0.4$ , and 1) high-entropy alloys with excellent heat-softening resistance, *Entropy* 20 (2018) 951.
- [43] O. El-Atwani, N. Li, M. Li, A. Devaraj, J. Baldwin, M.M. Schneider, D. Sobieraj, J.S. Wrobel, D. Nguyen-Manh, S.A. Maloy, E. Martinez, Outstanding radiation resistance of tungsten-based high-entropy alloys, *Sci. Adv.* 5 (2019) eaav2002.
- [44] X.F. Liu, Z.L. Tian, X.F. Zhang, H.H. Chen, T.W. Liu, Y. Chen, Y.J. Wang, L.H. Dai, “Self-sharpening” tungsten high-entropy alloy, *Acta Mater.* 186 (2020) 257–266.
- [45] Y. Jia, H. Chen, X. Liang, Microstructure and wear resistance of  $\text{CoCrNbNiW}$  high-entropy alloy coating prepared by laser melting deposition, *Rare Met.* 38 (2019) 1153–1159.
- [46] W.B. Liao, H. Zhang, Z.Y. Liu, P.F. Li, J.J. Huang, C.Y. Yu, Y. Lu, High strength and deformation mechanisms of  $\text{Al}_{0.3}\text{CoCrFeNi}$  high-entropy alloy thin films fabricated by magnetron sputtering, *Entropy* 21 (2019) 146.
- [47] N.A. Khan, B. Akhavan, C. Zhou, H. Zhou, L. Chang, Y. Wang, Y. Liu, M.M. Bilek, Z. Liu, High entropy nitride (HEN) thin films of  $\text{AlCoCrCu}_{0.5}\text{FeNi}$  deposited by reactive magnetron sputtering, *Surf. Coat. Technol.* 402 (2020) 126327.
- [48] N.A. Khan, B. Akhavan, Z. Zheng, H. Liu, C. Zhou, H. Zhou, L. Chang, Y. Wang, Y. Liu, L. Sun, M.M. Bilek, Z. Liu, Nanostructured  $\text{AlCoCrCu}_{0.5}\text{FeNi}$  high entropy oxide (HEO) thin films fabricated using reactive magnetron sputtering, *Appl. Surf. Sci.* 553 (2021) 149491.
- [49] G. Liu, Y. Wang, S. Li, X. Wang, Nano-deformation behavior of a thermally aged duplex stainless steel investigated by nanoindentation, FIB and TEM, *J. Mater. Eng. Perform.* 27 (2018) 4714–4721.
- [50] W. Li, D. Xie, D. Li, Y. Zhang, Y. Gao, P.K. Liaw, Mechanical behavior of high-entropy alloys, *Prog. Mater. Sci.* 118 (2021) 100777.
- [51] D.B. Miracle, O.N. Senkov, A critical review of high entropy alloys and related concepts, *Acta Mater.* 122 (2017) 448–511.
- [52] Y. Zhang, J.P. Liu, S.Y. Chen, X. Xie, P.K. Liaw, K.A. Dahmen, J.W. Qiao, Y.L. Wang, Serration and noise behaviors in materials, *Prog. Mater. Sci.* 90 (2017) 358–460.
- [53] Y. Zhang, Y.J. Zhou, J.P. Lin, G.L. Chen, P.K. Liaw, Solid-solution phase formation rules for multi-component alloys, *Adv. Eng. Mater.* 10 (2008) 534–538.
- [54] Q. Xing, Y. Zhang, Amorphous phase formation rules in high-entropy alloys, *Chin. Phys. B* 26 (2017) 018104.
- [55] X. Yang, Y. Zhang, Prediction of high-entropy stabilized solid-solution in multi-component alloys, *Mater. Chem. Phys.* 132 (2012) 233–238.
- [56] S. Guo, C. Ng, J. Lu, C.T. Liu, Effect of valence electron concentration on stability of fcc or bcc phase in high entropy alloys, *J. Appl. Phys.* 109 (2011) 103505.
- [57] Y. Zhang, Q. Xing, High entropy alloys-manufacturing routes, in: F.G. Caballero (Ed.), *Encyclopedia of Materials: Metals and Alloys*, Elsevier, MA, United States, 2022, pp. 327–338.
- [58] X. Yan, Y. Zhang, High-entropy films and compositional gradient materials, *Surf. Technol.* 48 (2019) 98–106.
- [59] B. Du, H.H. Liu, Y.H. Chu, Fabrication and characterization of polymer-derived high-entropy carbide ceramic powders, *J. Am. Ceram. Soc.* 103 (2020) 4063–4068.
- [60] Y. Li, S. Zhou, Y. Zhang, Future research directions and applications for high-entropy materials, in: J. Brechtl, P.K. Liaw (Eds.), *High-Entropy Materials: Theory, Experiments, and Applications*, Springer Nature Switzerland AG, Cham, Switzerland, 2021, pp. 721–763.
- [61] C. Oses, C. Toher, S. Curtarolo, High-entropy ceramics, *Nat. Rev. Mater.* 5 (2020) 295–309.
- [62] P. Zhang, L. Ye, F. Chen, W. Han, Y. Wu, T. Zhao, Stability, mechanical, and thermodynamic behaviors of  $(\text{TiZrHfTaM})\text{C}$  ( $\text{M}=\text{Nb}, \text{Mo}, \text{W}, \text{V}, \text{Cr}$ ) high-entropy carbide ceramics, *J. Alloy. Compd.* 903 (2022) 163868.
- [63] G. Wu, C. Liu, A. Brognara, M. Ghidelli, Y. Bao, S. Liu, X. Wu, W. Xia, H. Zhao, J. Rao, D. Ponge, V. Devulapalli, W. Lu, G. Dehm, D. Raabe, Z. Li, Symbiotic crystal-glass alloys via dynamic chemical partitioning, *Mater. Today* 51 (2021) 6–14.
- [64] R. Nambury S, L. Larry J, B. Barbara M, Measurement equivalence: a comparison of methods based on confirmatory factor analysis and item response theory, *J. Appl. Psychol.* 87 (2002) 517–529.